

Cite this: *J. Mater. Chem. A*, 2019, 7, 26020

# Solution-processed perovskite-colloidal quantum dot tandem solar cells for photon collection beyond 1000 nm<sup>†</sup>

Afsal Manekkathodi,<sup>‡a</sup> Bin Chen,<sup>‡b</sup> Junghwan Kim,<sup>§b</sup> Se-Woong Baek,<sup>b</sup> Benjamin Scheffel,<sup>b</sup> Yi Hou,<sup>b</sup> Olivier Ouellette,<sup>b</sup> Makhsud I. Saidaminov,<sup>b</sup> Oleksandr Voznyy,<sup>b</sup> Vinod E. Madhavan,<sup>a</sup> Abdelhak Belaidi,<sup>a</sup> Sahel Ashhab<sup>\*a</sup> and Edward Sargent<sup>\*b</sup>

Multi-junction solar cells based on solution-processed metal halide perovskites offer a route to increased power conversion efficiency (PCE); however, the limited options for infrared (IR)-absorbing back cells have constrained progress. Colloidal quantum dot (CQD)-based solar cells, which are solution-processed and have bandgaps tunable to wavelengths beyond 1000 nm, are attractive candidates for this role. Here we report a solution-processed four-terminal (4T) tandem solar cell comprised of a perovskite front cell and a CQD back cell. The 4T tandem provides a PCE exceeding 20%, the highest PCE reported to date for a perovskite-CQD tandem solar cell. The front semi-transparent perovskite solar cell employs a dielectric-metal-dielectric (DMD) electrode constructed from a metal film (silver/gold) sandwiched between dielectric (MoO<sub>3</sub>) layers. The highest-performing front semi-transparent perovskite solar cells exhibit a PCE of ~18%. By tuning the wavelength-dependent transmittance of the DMD layer based on the zero-reflection condition of optical admittance, we build semi-transparent perovskite solar cells with a 25% increase in IR transmittance compared to baseline devices. The back cell is fabricated based on an IR CQD absorber layer complementary to the IR transmittance of the semi-transparent perovskite front cell. Solution-processed hybrid tandem photovoltaics (PV) combining these technologies offer to contribute to higher-efficiency solar cells for next-generation flexible photovoltaic (PV) devices.

Received 7th September 2019  
Accepted 30th October 2019

DOI: 10.1039/c9ta11462a

rsc.li/materials-a

## Introduction

Multi-junction solar cells composed of complementary absorber layers with appropriate bandgaps offer avenues to improve the AM1.5 power conversion efficiency (PCE) beyond the Shockley-Queisser (SQ) limit of single-junction solar cells.<sup>1-4</sup> Photovoltaic (PV) technologies based on low-temperature solution processing have attracted interest in the pursuit of low-cost, flexible, and lightweight solar cells that could be part of multi-junction solar cell designs.<sup>1,5-7</sup>

Organic-inorganic metal halide perovskite-based solar cells have emerged as promising PV materials in the past decade and have made progress in PCE from 3.7% in 2009 to 25.2% today,

a figure that is rapidly approaching the PCE of silicon solar cells.<sup>8-12</sup> These perovskite materials are made using solution-based methods. The bandgap tunability of perovskite materials, from 1.2 to 2.3 eV, makes them of interest for tandem applications.

Significant efforts have been devoted to tandem devices in which perovskite solar cells were stacked with conventional PV technologies such as c-Si and CIGS (CuIn<sub>x</sub>Ga<sub>1-x</sub>Se<sub>2</sub>) to form hybrid tandem devices that provided PCEs of 25.2% and 23.4% respectively.<sup>1,4,13,14</sup> Demonstrations of perovskite-based tandem solar cells having a low-temperature and solution-processed back cell are limited. A major obstacle for all-solution-processed tandem cells has been the lack of an efficient, low-temperature-processed IR back-cell technology. Hybrid tandem solar cells obtained by combining a back cell with IR organic solar materials and front perovskite solar cells have seen significant progress in recent years towards low-cost and flexible PV technology.<sup>11,15-17</sup> Perovskite-organic tandem solar cells recently achieved an efficiency of 17.3% in a 2T configuration.<sup>15</sup> State-of-art solution-processed perovskite-perovskite tandem solar cells have demonstrated best PCEs of 25% and 23% for 4-terminal (4T) and 2-terminal (2T) device configurations, respectively.<sup>16,18-20</sup>

<sup>a</sup>Qatar Environment and Energy Research Institute, Hamad Bin Khalifa University, Qatar Foundation, Doha, Qatar. E-mail: sashhab@hbku.edu.qa

<sup>b</sup>Department of Electrical and Computer Engineering, University of Toronto, 35 St. George Street Toronto, Ontario, M5S 1A4 Canada. E-mail: ted.sargent@utoronto.ca

<sup>†</sup> Electronic supplementary information (ESI) available. See DOI: 10.1039/c9ta11462a

<sup>‡</sup> Authors with equal contribution.

<sup>§</sup> Present address: Photo-electronic Hybrids Research Center, Korea Institute of Science and Technology (KIST), Seoul 02792, Korea.

These back cell absorber materials require bandgap tunability below 1.2 eV to harness photons with wavelengths beyond  $\sim 1000$  nm. IR perovskite absorber materials have been developed by varying the B-site cations in the  $ABX_3$  perovskite structure, replacing lead with tin to yield a bandgap as low as 1.2 eV. Tin-based perovskites are prone to oxidation and hysteresis, and further adjusting the bandgap below 1.2 eV has proven challenging.<sup>1,21</sup>

Colloidal quantum dots (CQDs) can reach bandgaps as low as 0.5 eV, offering therefore a path to harness photons in the near-infrared (NIR) and short-wavelength infrared (SWIR) regions of the solar spectrum, beyond the range of silicon and perovskites.<sup>3,22–24</sup> CQDs are low-temperature-solution-processed materials with a size-tuned bandgap. Previous attempts to fabricate perovskite:CQD two-terminal (2T) tandem cells have recently reached a PCE of 11%.<sup>24,25</sup> These PCEs are lower than those of the single-junction perovskite cells used as front cells. In this work, we achieved 4T tandem solar cells having stabilized PCEs of 20.2%, where the device employed a perovskite front cell and a CQD back cell. This is the highest PCE reported for a perovskite:CQD tandem solar cell, and it surpasses the performance of both the perovskite and the CQD single-junction control solar cells employing reflective back contacts.

The 4T hybrid tandem solar cell design avoids complexities such as combining mutually aggressive solution processing methods and current-matching conditions.<sup>1,2,13</sup> Challenges in designing high-performance solution-processed 4T tandem cells include the development of an efficient semi-transparent perovskite solar cell; the fabrication of an indium-free transparent electrode exhibiting enhanced IR light transmission and providing compatibility with the perovskite solar cell; and the design of a spectrally-matched stable back cell in the IR range. Here the semi-transparent front cell exploits a dielectric-metal-dielectric transparent conducting electrode (DMD-TCE) that contains ultrathin Au/Ag metal films sandwiched between dielectric  $MoO_3$  layers. The DMD structure is designed based on the zero-reflection condition in the optical admittance diagram, an approach that allows us to improve IR transmittance compared to the case of conventional DMDs in which visible light transmittance is enhanced at the cost of suppressing IR transmittance.<sup>26</sup>

Detailed-balance calculations<sup>27</sup> (Fig. 1a) indicate that, in the limit of high performance, a theoretical PCE of  $\sim 45\%$  is available by stacking 1.75 eV and 0.9 eV bandgap absorbing materials under 1-sun illumination. Experimentally, we mechanically stacked (Fig. 1b) 1.63 eV bandgap semi-transparent front cells atop 1.15 eV bandgap CQD back cells. The back cells exploit CQD absorber layers with IR light trapping; their absorption spectra are complementary to the transmission from the front perovskite cells to optimize tandem performance. The photocurrent extraction potential of the PbS CQDs (0.95 eV) in the IR region in the solar irradiance spectrum is shown in Fig. 1c.

An efficient 4T tandem requires a high-performance semi-transparent perovskite solar cell with the enhanced light transmission in the IR region in the solar spectrum.<sup>13,16,19</sup> Low-temperature ( $\leq 150$  °C) processed planar perovskite solar cells were adopted for the perovskite cell. The opaque control perovskite cell of the desired bandgap is optimized at the outset. These cells were in the following device architecture: indium tin oxide (ITO)/electron transport layer (ETL)/perovskite absorber layer/Spiro-OMeTAD based hole-transport layer (HTL)/gold (Au). The electron transport layers used are low temperature processed  $SnO_2$ , while the perovskite absorbers are based on a stable 3-cation (FA, MA, and Cs) perovskite with  $Cs_{0.05}MA_{0.10}FA_{0.85}PbI_{0.85}Br_{0.15}$  composition and a bandgap of  $\sim 1.63$  eV.

Fig. 2a shows a schematic of the device architecture of the semi-transparent (semi-t) solar cells that use a DMD-TCE to replace the conventional gold back electrode. We explored different metals such as gold, silver, and gold-catalyzed silver in the DMD architecture to obtain conformally-coated ultra-thin metal films with increased conductivity. We used 5 nm- $MoO_3$ /1 nm-Au/5 nm-Ag/35 nm- $MoO_3$  as the DMD layers; these were deposited using thermal/e-beam evaporation. The first  $MoO_3$  layer used was 5 nm in thickness to improve current extraction; thicker  $MoO_3$  layers reduce the current by adding series resistance. The best PV performance for the semi-transparent devices was obtained with 1 nm gold-catalyzed 5 nm silver films, which have a sheet resistance of  $\sim 30 \Omega \text{ sq}^{-1}$ . A 1 nm thin gold layer was deposited to catalyze the formation of a uniform and continuous ultra-thin silver film through reduced

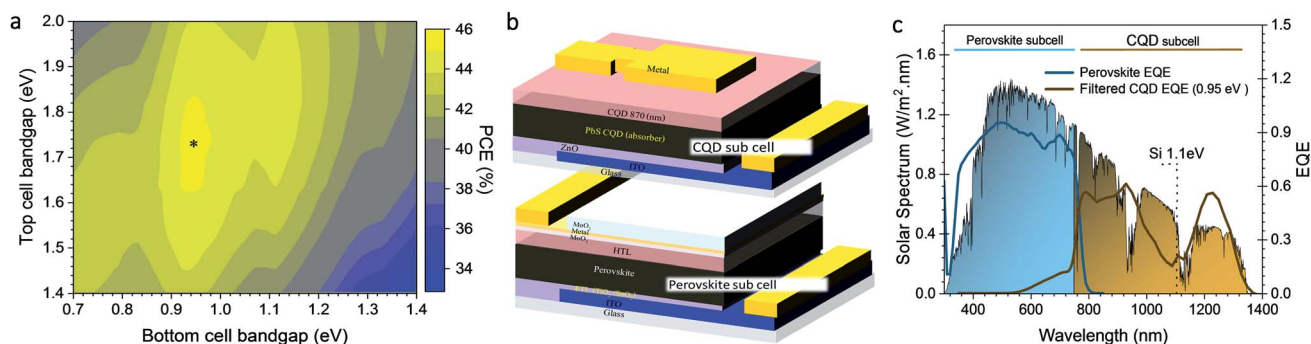


Fig. 1 Perovskite-CQD tandem design. (a) Calculated PCE detailed-balance limit for the hybrid 4T tandem solar cell as a function of front cell and back cell bandgaps. (b) Schematic of a 4T device. (c) Solar irradiance spectrum matched to the spectral regions of the perovskite and CQD absorber materials; the EQE shows the corresponding photocurrent extraction potential in tandem applications.

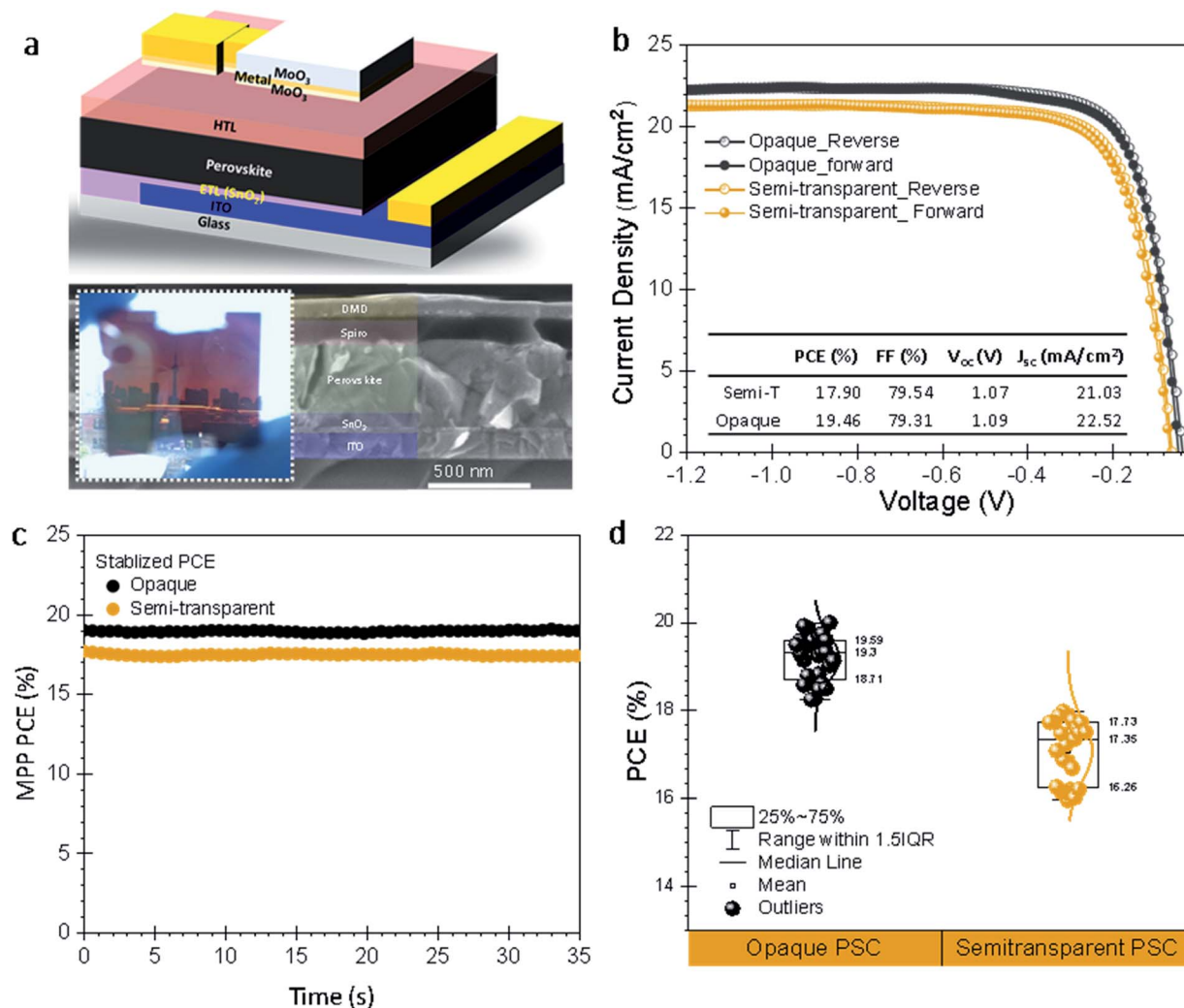


Fig. 2 Semi-transparent perovskite devices and performance. (a) Schematic of device architecture, cross-section scanning electron microscope image, and a photograph of the semi-transparent perovskite solar cell. (b) *JV* characteristic of SnO<sub>2</sub>-based opaque and semi-transparent devices showing 19.5% and 17.9% PCE under the illumination of 100 mW cm<sup>-2</sup> light. (c) Stabilized PCE measured at the maximum power point. (d) Histograms of PCE for semi-transparent and opaque perovskite solar cells.

percolation and enhanced adhesion at the MoO<sub>3</sub> interface.<sup>28</sup> The conformal formation of the ultra-thin Ag film is dictated by the layer-by-layer nucleation in the Au/Ag heterostructure according to the Frank-van der Merwe growth mode.<sup>11,29</sup> The top MoO<sub>3</sub> film is optimized for IR transmittance.

In the semi-transparent perovskite solar cells, we used SnO<sub>2</sub> as the ETL. SnO<sub>2</sub> exhibits performance superior to that of the conventional TiO<sub>2</sub> ETL due to its better band alignment, higher electron mobility and lower trap state density that facilitate better extraction without carrier accumulation at the SnO<sub>2</sub>/perovskite interface.<sup>30,31</sup> SnO<sub>2</sub>-based control non-transparent perovskite solar cells were optimized to have stabilized PCE of 18.9% (ESI, Fig. S1†). The gold contact was replaced with the DMQ-TCE as back contact for the semi-transparent perovskite solar cells. The best semi-transparent perovskite solar cells yielded a stabilized PCE of 17.6%, as shown in Fig. 2b and c. The hysteresis effect was negligible in both opaque and semi-transparent devices. This is one of the highest PCEs reported

among semi-transparent perovskite solar cells.<sup>18,19</sup> The EQE spectra of both the opaque and the semi-transparent perovskite solar cells agree well with the corresponding *JV* measurements. Compared with the opaque devices, the semi-transparent devices showed ~1–2 mA cm<sup>-2</sup> photocurrent loss caused by the single-pass optical losses through the DMQ TCE (ESI, Fig. S2†).

Design and optimization of the TCE for high conductivity and wavelength-selective light transmittance is required to realize high-performance tandem photovoltaic devices. Highly conductive IR transmitting TCEs maximizes the PV performance of the back CQD solar cell.<sup>13,19,26,32</sup> DMQ-based TCEs have advantages over conventional transparent conducting oxides (TCOs) in their simplicity, low-temperature processing, their avoidance of reliance on indium, and their compatibility with perovskite-based solar cells.

In prior DMQ optimizations, visible-light transmittance has been optimized at the expense of IR transmittance, since

organic light-emitting diodes (OLEDs), power-generating windows, and transparent heat-reflection film applications benefit from meeting such high-visible-transmittance specifications.<sup>26,33,34</sup> In a DMD-TCE, the optical transmittance is enhanced by selecting dielectric materials with  $\epsilon_{\text{dielectric}} > \epsilon_{\text{metal}}$  in order to suppress surface plasmonic loss in the metal film. These dielectric materials also protect metal films from oxidation and degradation.<sup>33</sup> These dielectric materials also protect metal films from oxidation and degradation.

Here we optimized the DMD instead to maximize IR transmittance for tandem PV applications. We first estimated the IR optical transmittance of the DMD structure using the transfer-matrix method (TMM), as shown in Fig. 3a.<sup>35</sup> The results suggest that the average optical transmittance can be increased through control over the thickness of the top dielectric film. Distinctive spectrally-dependent optical transmission characteristics are observed in the visible and IR regions as a function of the thickness of the top oxide (ESI, Fig. S3†). Simulations indicate that the maximum transmittance for the DMD

structure in the visible range (400–750 nm) is achieved for a MoO<sub>3</sub> thickness of ~30 nm while that of the IR region (750–1400 nm) is achieved at ~60 nm (ESI, Fig. S3†). The experimental results on the transmittance of the DMD structures on glass followed the same trend. The average transmittance in the IR range showed the best transmittance with a ~50 nm thick top oxide (ESI, Fig. S4†).

Fine-tuning of the DMD structure for better light management in the IR region is achieved by following the zero-reflection condition using optical admittance diagram.<sup>36</sup> The inset of Fig. 3b shows a MoO<sub>3</sub>/Ag/MoO<sub>3</sub> DMD system on the glass substrate, where light enters through the glass substrate and exits at the MoO<sub>3</sub>/Air interface. Its admittance consists of three connected curves (representing each layer in the DMD structure) tracing clockwise, starting from the complex refractive index of air (1, 0) and ending at that of the glass substrate (1.52, 0) to obtain the zero-reflection condition. As the top layer MoO<sub>3</sub> thickness increases, its admittance curve (yellow line) intersects that of Ag (green line). Then the admittance follows

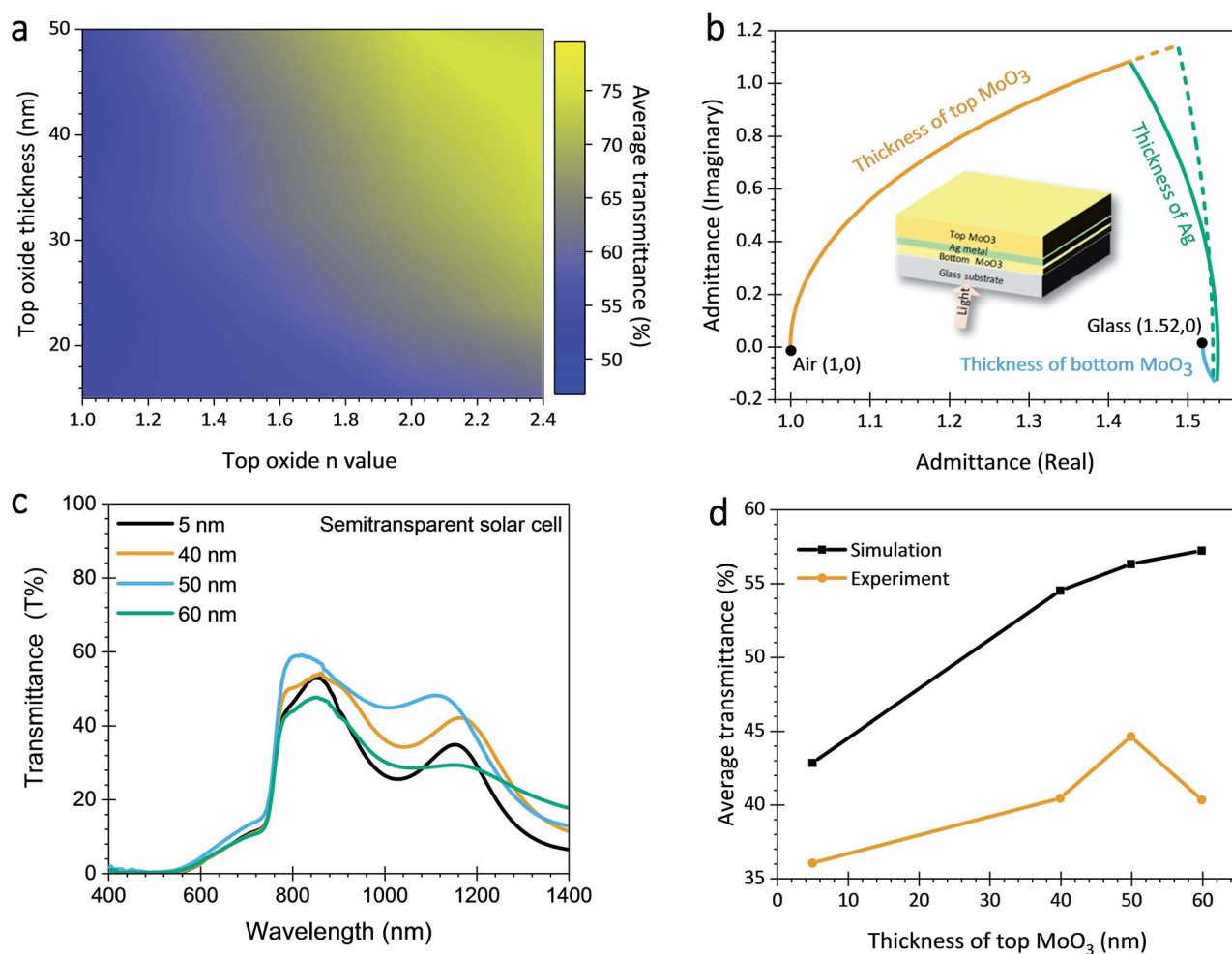


Fig. 3 DMD design for optimized IR transparency. (a) IR transmittance as a function of the thickness and refractive index of the top oxide in the DMD structure. (b) Admittance diagram of the MoO<sub>3</sub>/Ag/MoO<sub>3</sub> thin film structure. The solid and dashed lines are for 600 nm and 1000 nm wavelength incident light, respectively. (c) Transmittance spectrum of the semi-transparent perovskite solar cell based on SnO<sub>2</sub> ETL. (d) Calculated and experimental average transmittance of semi-transparent perovskite solar cell in the 750–1400 nm region.

the curve for silver until it intersects the admittance curve for the bottom MoO<sub>3</sub> layer. Finally, the curve further extends to intersect with the real axis at (1.52, 0), completing the zero-reflection admittance curve.

Since the refractive index is wavelength-dependent, the optical admittance of the DMD structure varies with incident photon energy. In particular, the refractive index of MoO<sub>3</sub> does not have a significant spectral dependence, whereas the

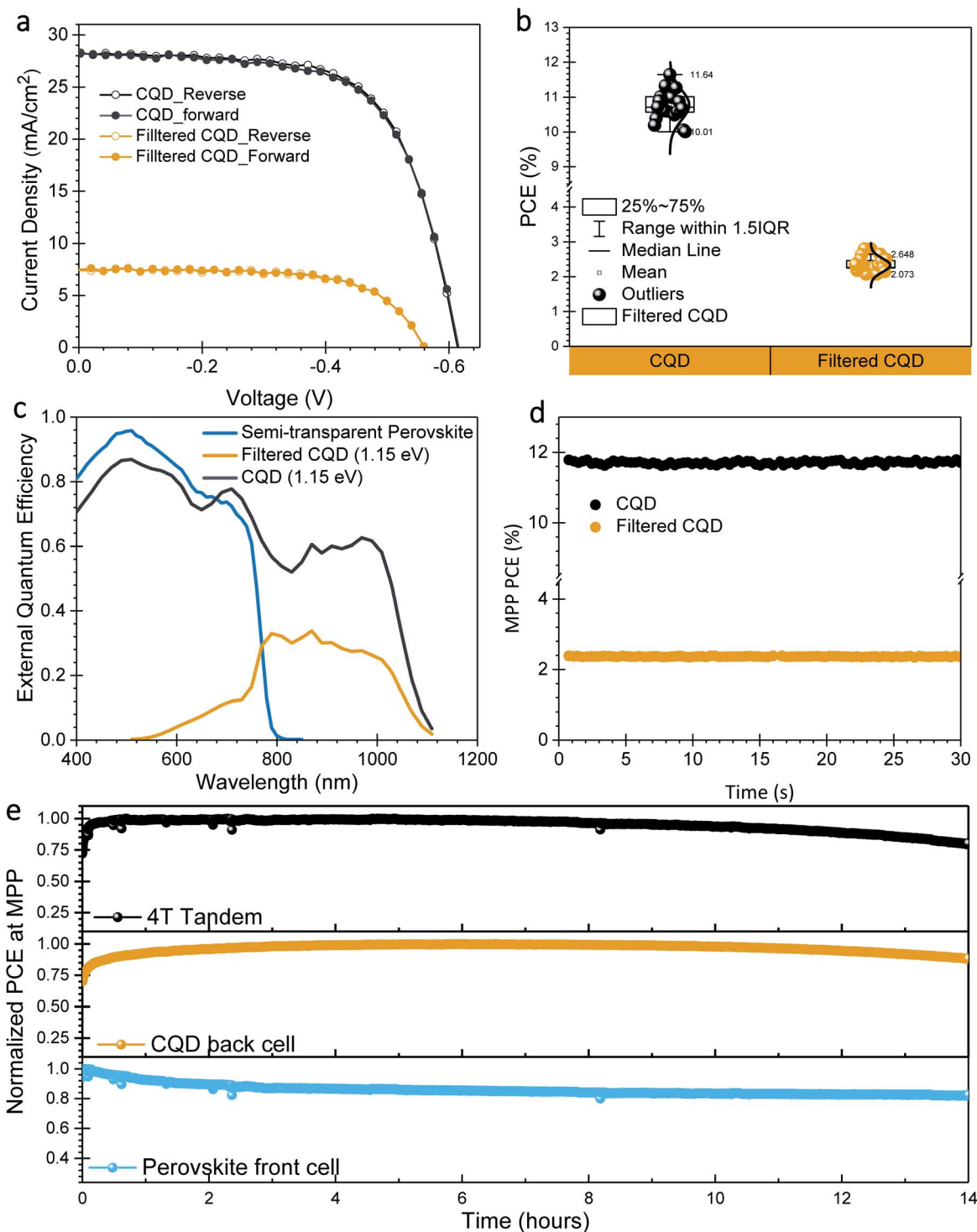


Fig. 4 Photovoltaic performance of CQD solar cells and 4T tandem devices. (a) JV characteristics of unfiltered and filtered IR CQD devices using semi-transparent front perovskite solar cells under 100 mW cm<sup>-2</sup> illumination. (b) Histogram of device PCEs for CQD and filtered CQD devices. (c) EQE spectra collected from the front perovskite cell and back CQD cells. The black curve is the EQE spectrum recorded from unfiltered CQD device (d) The stabilized PCE of the CQD and filtered CQD cells measured at the maximum power point and (e) MPP tracking of the semi-transparent front perovskite cell, filtered back CQD cell, and the 4T tandem device under simulated AM 1.5G one-sun illumination.

extinction coefficient of the silver film increases significantly at longer wavelengths (ESI, Fig. S5†). This requires a thicker top MoO<sub>3</sub> film for higher IR transmittance, achieved by bringing the admittance of the DMD structure back to the zero-reflection condition, as shown in Fig. 3b. The dashed lines represent the admittance to light at 1000 nm wavelength, in which the top MoO<sub>3</sub> needs to increase its thickness to reach the curve of Ag, compared to the admittance curve for the light at 600 nm wavelength. The transmittance of semi-transparent devices also follows the same trend. Fig. 3c shows the overall device transmittance of SnO<sub>2</sub>-based semi-transparent solar cells, which enhances the transmittance depending on the thickness of the top oxide similarly to the DMD transmittance. For the 50 nm top oxide, maximum transparency of 56% is achieved at 800–900 nm wavelength and an average IR transmittance of ~46% is reached in the IR wavelength range (750–1400 nm).

In the next step in designing efficient 4T tandem solar cells, we fabricated (on ITO-coated glass substrates) PbS IR CQD solar cells as the back cell. The CQD solar cells consist of zinc oxide (ZnO) as the electron transport layer, a PbS CQD active layer, 1,2-ethanedithiol (EDT)-treated PbS CQDs as the hole transport layer, and E-beam evaporated gold as the back electrode. PbS CQDs with bandgaps of ~1.15 eV and ~0.95 eV were chosen as the main absorber layers in this study since they best match the transmittance of the perovskite front cell. PbS CQDs were first passivated using PbX (X = I, Br) *via* a solution-phase ligand exchange and then spin-coated.<sup>23,37</sup> Following IR CQD deposition, two layers of EDT-treated wide-bandgap (860 nm) PbS CQDs were deposited onto the CQD film. To maximize the CQD-perovskite tandem cell efficiency, it is important to maximize the photocurrent harvesting of IR light beyond 750 nm in the back CQD solar cells. This is achieved by increasing the thickness of the CQD active layer to extract the maximum photocurrent in the IR region (ESI, Table ST1†). EQE measurements of 1.15 eV and 0.95 eV CQD absorbers showed high EQE values at the exciton peaks; which indicates that the solar cells have an excellent IR charge collection efficiency from light absorbed beyond 750 nm (ESI, Fig. S7†). EQE measurements also showed that ~46% of the total extractable photons incident on the back CQD cells are utilized in these tandem devices. These results suggest that it is possible to extract a cumulative current density of ~11.6 mA cm<sup>-2</sup> (1.15 eV) and 15.2 mA cm<sup>-2</sup> (0.95 eV) if one neglects parasitic absorption loss in the DMD layer. Though the current extraction is increased when using the 0.95 eV CQDs,

this is accompanied by a reduction in the open-circuit voltage, resulting in no significant benefit in reducing the bandgap within this 4T design.

The CQD-perovskite 4-terminal tandem is implemented by stacking the PbS-CQD solar cell as the back cell behind the semi-transparent perovskite front cell. The measurements were carried out by following previously reported methods for 4T solar cells.<sup>13,18,19</sup> The efficiencies of the individual cells were evaluated and the sum of these two yields the overall PCE of the tandem cell.<sup>18,19</sup> The *JV* curves of the CQD cell, measured with and without the semi-transparent perovskite cell in front, are shown in Fig. 4a. Histograms are provided in Fig. 4b. When the semi-transparent front cell, with its stabilized PCE of 17.6%, is in place, the back cell adds 2.6% absolute power points. In this case, the best performing 4T tandem achieves a 20.2% stabilized power conversion efficiency (Table 1). The hysteresis in the PbS-CQD based bottom solar cell is negligible. The *J*<sub>sc</sub> measured from the *J-V* curve of the filtered back cell (7.0 mA cm<sup>-2</sup>) is consistent with the *J*<sub>sc</sub> calculated from the EQE spectrum.

We evaluated the stability of the semi-transparent perovskite solar cells, the CQD back cells, and the corresponding 4T tandem devices, by using maximum power point (MPP) tracking under simulated AM 1.5G one-sun illumination. The MPP tracking of these solar cells was carried out without encapsulation. The semi-transparent perovskite solar cells showed a constant rate of degradation (Fig. 4e), wherein about 15% of the initial efficiency was lost following 14 hours MPP tracking. The CQD devices showed a small initial increase (1–3.5 hours). The 4T tandem devices showed an MPP degradation with time, with the PCE decreasing to 90% of its maximum value after our measurement time of 12.5 hours.

Further progress is available in perovskite-CQD tandems *via* concurrent advances in light management in perovskite sub-cells and enhanced IR charge collection in CQD sub-cells. Better light management can be accomplished by making semi-transparent perovskite solar cells with wider bandgaps and employing an asymmetric oxide-based multilayer DMD design or by using an IR-transparent conductive oxide. Innovative strategies used in CQD device fabrication, such as combining multiple bandgap CQD ensembles<sup>38</sup> or using graded architectures,<sup>37</sup> can enhance the filtered current extraction from the back CQD solar cell to approach more closely the full potential of this solution-processed tandem PV technology.

Table 1 Summary of photovoltaic performances of the 4T perovskite CQD tandem solar cells

		<i>V</i> <sub>oc</sub> (V)	<i>J</i> <sub>sc</sub> (mA cm <sup>-2</sup> )	FF (%)	PCE (%)	Stabilized PCE (%)
Semi-transparent perovskite front cell	Reverse	1.07	21.03	79.56	17.90	17.6
	Forward	1.07	20.89	78.97	17.65	
Unfiltered CQD back cell	Reverse	0.64	29.41	62.0	11.67	11.6
	Forward	0.64	28.98	61.64	11.61	
Filtered CQD back cell	Reverse	0.58	7.13	65.2	2.65	2.6
	Forward	0.58	6.96	64.2	2.63	
<b>4T tandem (perovskite + CQD)</b>					<b>20.55</b>	<b>20.2</b>
					<b>20.28</b>	

## Conclusions

We demonstrate solution-processed hybrid tandem PV devices combining two emerging types of photoabsorbing materials, perovskites and CQDs. The 4T tandem solar cell achieved a stabilized efficiency of 20.2% based on a perovskite front cell and a CQD back cell. An ultrathin DMD layer as part of the perovskite solar cells gave semi-transparent solar cells with stabilized PCEs of  $\sim 18\%$  for champion cells, among the highest PCEs reported for semi-transparent solar cells and well-suited to serve as the front cell in a 4T tandem devices. This DMD-TCE, which contains an ultrathin Au/Ag metal film sandwiched between dielectric  $\text{MoO}_3$  layers, has a wavelength-dependent transmittance which we took into consideration when we optimized it for maximum IR transmittance as needed for the tandem design. The CQD solar cell achieved a PCE of 11.3% under unfiltered solar illumination and a PCE when it functioned as the back cell 2.6% behind the perovskite front cell. These results demonstrate CQD and perovskite solar cells as a promising combination for solution-processed tandem solar cells for next-generation photovoltaic technologies.

## Experimental

### Materials

All the materials were used as received without purification. Pre-patterned ITO substrates ( $20 \Omega \text{ sq}^{-1}$ ) with  $25 \text{ mm} \times 25 \text{ mm}$  dimension were purchased from TFD inc.  $\text{PbI}_2$  beads (99.999%),  $\text{PbBr}_2$  (99.999%),  $\text{CsI}$  (99.999%), and  $\text{MoO}_3$  powders were purchased from Alfa Aesar. Methylammonium iodide (MAI), formamidinium iodide (FAI), methylammonium bromide (MABr) were purchased from GreatCell Solar. The  $\text{SnO}_2$  nanoparticle was bought from Alfa Aesar. All the solvent used in the process were anhydrous solvents and purchased from Sigma-Aldrich.

**Electron-transport layer (ETL) fabrication.** Patterned ITO/glass substrates were cleaned with deionized water, acetone, and isopropanol, respectively. The precursor for  $\text{SnO}_2$  layer fabrication was prepared by diluting (1 : 6 ratio) the  $\text{SnO}_2$  nanoparticles solution (Alfa Aesar) in deionized water. This solution is spin-coated on the ITO substrates with 3000 rpm for 15 s and annealed at  $150^\circ\text{C}$  for 30 minutes. This was transferred to the  $\text{N}_2$  glovebox immediately when cooled down to room temperature.

**Perovskite absorber layer fabrication.** The perovskite absorber layers were deposited inside the  $\text{N}_2$ -filled glove box with a controlled  $\text{H}_2\text{O}$  and oxygen level to less than 1 PPM. The temperature inside was monitored to be  $25\text{--}30^\circ\text{C}$ . The glove box was purged after the fabrication of every 8 samples to remove the solvent ambience in the glove box. The precursors for  $\text{Cs}_{0.05}\text{MA}_{0.10}\text{FA}_{0.85}\text{PbI}_{0.85}\text{Br}_{0.15}$  perovskites were prepared by dissolving the  $\text{PbI}_2$ ,  $\text{PbBr}_2$ ,  $\text{CsI}$ , FAI, and MABr in DMF : DMSO (4 : 1 in volume) solvents. The perovskite films were deposited on to the  $\text{SnO}_2$  coated ITO substrates following a two-step spin-coating procedure. The substrate was spun at 1000 rpm for 10 s with an acceleration of 200 rpm at first, and at 6000 rpm for the 30 s with an acceleration of 2000 rpm in the second step. In the

second step, 200  $\mu\text{L}$  chlorobenzene was dropped onto the substrate after 25 seconds. The substrate was immediately placed on a hotplate and annealed at  $100^\circ\text{C}$  for 30 minutes.

**Hole-transport layer (HTL) fabrication.** The HTM (Spiro-OMeTAD) was deposited immediately after fabrication of perovskite films. Spiro-OMeTAD solution was prepared by dissolving 65 mg SpiroOMeTAD in 1 mL Chlorobenzene. Then 70  $\mu\text{L}$  lithium bis(trifluoromethane)sulfonimide salt solution ( $170 \text{ mg mL}^{-1}$  in acetonitrile) and 20  $\mu\text{L mL}^{-1}$  *tert*-butylpyridine were added. This solution was spun at 4000 rpm for 20 seconds on perovskite films. Then the samples were kept in ambient environment overnight at dark for oxidation.

**Back electrode fabrication.** 120 nm Au film was deposited atop the Spiro-OMeTAD by electron-beam evaporation as a back contact electrode for opaque perovskite solar cell. The device area ( $0.053 \text{ cm}^2$ ) is defined by a deposition mask. The multi-layered DMD architectures ( $\text{MoO}_3/\text{Au}/\text{Ag}/\text{MoO}_3$ ) were deposited sequentially. The silver and  $\text{MoO}_3$  was deposited using the thermal evaporation. The  $\text{MoO}_3$  and 1 nm-gold were deposited at a rate of  $0.2 \text{ \AA s}^{-1}$ . Then, 5 nm-silver was deposited on the 1 nm gold at a rate of  $2 \text{ \AA s}^{-1}$ . Finally, the top  $\text{MoO}_3$  was thermally evaporated at a rate of  $0.5 \text{ \AA s}^{-1}$ .

### PbS colloidal-quantum dot solar cell fabrication

Patterned ITO/glass substrates were cleaned with detergent, deionized water, acetone, and isopropanol respectively. A compact ZnO thin film was spin-coated on substrate as ETL. For making CQD absorber layers, a halide ligand-exchanged quantum dot was spun into the ZnO film. The halide-ligand exchange process was carried out by mixing PbS quantum dot with ligand (PBI, PbBr, ammonium acetate) solution in octane. After the ligand exchange, CQDs were washed with octane and separated by centrifugation with the addition of toluene. These dried PbS CQDs were re-dispersed in butylamine for spin coating. After the IR CQD deposition, two layers of EDT-treated wide bandgap (860 nm) PbS CQDs were deposited on to the absorber CQD film. Finally, an Au electrode of 120 nm was deposited by e-beam at  $2 \text{ \AA s}^{-1}$ .

**Solar cell performance measurement and characterization.** The  $J$ - $V$  characteristics of the solar cells were measured using a Keithley 2400 source meter under a simulated AM1.5G solar spectrum (Sciencetech, class AAA) from a Xe-lamp (Solar Light Company Inc.). The irradiation power was calibrated with a reference Si solar cell (Newport, Inc.) at  $100 \text{ mW cm}^{-2}$ . The active area ( $0.049 \text{ cm}^2$ ) was determined by the aperture mask. The samples were under constant  $\text{N}_2$  flow at room temperature using a custom-built measurement setup. The  $J$ - $V$  measurements were performed in forward and reverse directions at a rate of  $50 \text{ mV s}^{-1}$ . The stabilized power output was obtained by setting the bias voltage to the initial  $V_{\text{MPP}}$  that was determined from the  $JV$  curve. We used previously reported 4T measurement protocol to measure the performance of our tandem cells<sup>18,19</sup> CQD back cells were measured under the semi-transparent perovskite cell filters. During the 4T measurement, back cell device area was covered by a larger ( $2 \text{ cm} \times 2 \text{ cm}$ ) semi-transparent perovskite cell filters, fabricated in the same batch

and procedure as that of the actual devices. The filtered PCE of CQD using a small area (0.053 cm<sup>2</sup>) and large area (2 cm × 2 cm) filters are the same as shown in Fig. S8.†

EQE-spectra were measured under monochromatic illumination from a 400W Xe-lamp. A Newport 818-UV and Newport 838-IR sensors were used for calibration. The current response was collected at short-circuit conditions with a Lakeshore preamplifier connected to a Stanford Research 830 lock-in amplifier. The total absorption and transmittance were extracted from the reflection and *via* a UV-vis-IR spectrophotometer (Lambda 950). Cross-sectional imaging of the devices was obtained by field-emission scanning electron microscopy (3 kV).

**4T performance simulation.** The theoretical efficiency was estimated by detailed-balance calculations.<sup>27</sup> The short-circuit current was calculated by integrating the AM1.5G spectrum assuming 100% EQE above the bandgap. The reverse saturation current was calculated from detailed balance,<sup>27</sup> assuming 100% radiative recombination. From these quantities, an *I*-*V* curve was simulated assuming the ideal diode equation.

**Optical modeling.** Calculations were carried out by using open-source transfer matrix code.<sup>39</sup> Optical constants of each layer were measured using spectroscopic ellipsometry (ESI S5 and S6†). Spectroscopic ellipsometry was performed using a Horiba UVISEL Plus extended range ellipsometer with a 200 ms integration time, a 5 nm step size and a 1 mm diameter spot size at an incident angle of 70 degrees. Soda-lime glass slides were used as substrates for each material, with their back covered with cloudy adhesive tape to ensure back-reflections are diffusively reflected away from the detector. Fitting was performed using Horiba's DeltaPsi2 dedicated software.

## Conflicts of interest

There are no conflicts to declare.

## Acknowledgements

This work was made possible by NPRP grant #8-086-1-017 from the Qatar National Research Fund. This research was also supported by Ontario Research Fund-Research Excellence program (ORF7-Ministry of Research and Innovation, Ontario Research Fund-Research Excellence Round 7); and by the Natural Sciences and Engineering Research Council (NSERC) of Canada. The findings achieved herein are solely the responsibility of the authors. The authors thank Mohamed I. Helal (Core labs, QEERI) for help with SEM characterizations.

## References

- 1 T. Leijtens, K. A. Bush, R. Prasanna and M. D. McGehee, *Nat. Energy*, 2018, **3**, 828–838.
- 2 G. E. Eperon, M. T. Hörantner and H. J. Snaith, *Nat. Rev. Chem.*, 2017, **1**, 0095.
- 3 E. H. Sargent, *Nat. Photonics*, 2012, **6**, 133.
- 4 N. N. Lal, Y. Dkhissi, W. Li, Q. Hou, Y.-B. Cheng and U. Bach, *Adv. Energy Mater.*, 2017, **7**, 1602761.
- 5 J. Jean, J. Xiao, R. Nick, N. Moody, M. Nasilowski, M. Bawendi and V. Bulović, *Energy Environ. Sci.*, 2018, **11**, 2295–2305.
- 6 A. R. Uhl, A. Rajagopal, J. A. Clark, A. Murray, T. Feurer, S. Buecheler, A. K. Y. Jen and H. W. Hillhouse, *Adv. Energy Mater.*, 2018, **8**, 1801254.
- 7 M. Li, K. Gao, X. Wan, Q. Zhang, B. Kan, R. Xia, F. Liu, X. Yang, H. Feng, W. Ni, Y. Wang, J. Peng, H. Zhang, Z. Liang, H.-L. Yip, X. Peng, Y. Cao and Y. Chen, *Nat. Photonics*, 2016, **11**, 85.
- 8 A. Kojima, K. Teshima, Y. Shirai and T. Miyasaka, *J. Am. Chem. Soc.*, 2009, **131**, 6050–6051.
- 9 V. E. Madhavan, I. Zimmermann, C. Roldán-Carmona, G. Grancini, M. Buffiere, A. Belaidi and M. K. Nazeeruddin, *ACS Energy Lett.*, 2016, **1**, 1112–1117.
- 10 H. Tan, A. Jain, O. Voznyy, X. Lan, F. P. García de Arquer, J. Z. Fan, R. Quintero-Bermudez, M. Yuan, B. Zhang, Y. Zhao, F. Fan, P. Li, L. N. Quan, Y. Zhao, Z.-H. Lu, Z. Yang, S. Hoogland and E. H. Sargent, *Science*, 2017, **355**, 722.
- 11 Y. Yang, Q. Chen, Y.-T. Hsieh, T.-B. Song, N. D. Marco, H. Zhou and Y. Yang, *ACS Nano*, 2015, **9**, 7714–7721.
- 12 Best Research-Cell Efficiency Chart | Photovoltaic Research | NREL, <https://www.nrel.gov/pv/cell-efficiency.html>.
- 13 H. Shen, T. Duong, J. Peng, D. Jacobs, N. Wu, J. Gong, Y. Wu, S. K. Karuturi, X. Fu, K. Weber, X. Xiao, T. P. White and K. Catchpole, *Energy Environ. Sci.*, 2018, **11**, 394–406.
- 14 F. Sahli, J. Werner, B. A. Kamino, M. Bräuninger, R. Monnard, B. Paviet-Salomon, L. Barraud, L. Ding, J. J. Diaz Leon, D. Sacchetto, G. Cattaneo, M. Despeisse, M. Boccard, S. Nicolay, Q. Jeangros, B. Niesen and C. Ballif, *Nat. Mater.*, 2018, **17**, 820–826.
- 15 L. Meng, Y. Zhang, X. Wan, C. Li, X. Zhang, Y. Wang, X. Ke, Z. Xiao, L. Ding, R. Xia, H.-L. Yip, Y. Cao and Y. Chen, *Science*, 2018, **361**, 1094.
- 16 D. Zhao, C. Wang, Z. Song, Y. Yu, C. Chen, X. Zhao, K. Zhu and Y. Yan, *ACS Energy Lett.*, 2018, **3**, 305–306.
- 17 G. Shi, Y. Wang, Z. Liu, L. Han, J. Liu, Y. Wang, K. Lu, S. Chen, X. Ling, Y. Li, S. Cheng and W. Ma, *Adv. Energy Mater.*, 2017, **7**, 1602667.
- 18 J. Tong, Z. Song, D. H. Kim, X. Chen, C. Chen, A. F. Palmstrom, P. F. Ndione, M. O. Reese, S. P. Dunfield, O. G. Reid, J. Liu, F. Zhang, S. P. Harvey, Z. Li, S. T. Christensen, G. Teeter, D. Zhao, M. M. Al-Jassim, M. F. A. M. van Hest, M. C. Beard, S. E. Shaheen, J. J. Berry, Y. Yan and K. Zhu, *Science*, 2019, eaav7911, DOI: 10.1126/science.aav7911.
- 19 D. Zhao, Y. Yu, C. Wang, W. Liao, N. Shrestha, C. R. Grice, A. J. Cimaroli, L. Guan, R. J. Ellingson, K. Zhu, X. Zhao, R.-G. Xiong and Y. Yan, *Nat. Energy*, 2017, **2**, 17018.
- 20 D. Zhao, C. Chen, C. Wang, M. M. Junda, Z. Song, C. R. Grice, Y. Yu, C. Li, B. Subedi, N. J. Podraza, X. Zhao, G. Fang, R.-G. Xiong, K. Zhu and Y. Yan, *Nat. Energy*, 2018, **3**, 1093–1100.
- 21 C. Wang, Z. Song, C. Li, D. Zhao and Y. Yan, *Adv. Funct. Mater.*, 2019, 1808801.
- 22 M. Liu, O. Voznyy, R. Sabatini, F. P. García de Arquer, R. Munir, A. H. Balawi, X. Lan, F. Fan, G. Walters,

- A. R. Kirmani, S. Hoogland, F. Laquai, A. Amassian and E. H. Sargent, *Nat. Mater.*, 2016, **16**, 258.
- 23 Z. Ning, O. Voznyy, J. Pan, S. Hoogland, V. Adinolfi, J. Xu, M. Li, A. R. Kirmani, J.-P. Sun, J. Minor, K. W. Kemp, H. Dong, L. Rollny, A. Labelle, G. Carey, B. Sutherland, I. Hill, A. Amassian, H. Liu, J. Tang, O. M. Bakr and E. H. Sargent, *Nat. Mater.*, 2014, **13**, 822.
- 24 A. Karani, L. Yang, S. Bai, M. H. Futscher, H. J. Snaith, B. Ehrler, N. C. Greenham and D. Di, *ACS Energy Lett.*, 2018, **3**, 869–874.
- 25 Y. Zhang, M. Gu, N. Li, Y. Xu, X. Ling, Y. Wang, S. Zhou, F. Li, F. Yang, K. Ji, J. Yuan and W. Ma, *J. Mater. Chem. A*, 2018, **6**, 24693–24701.
- 26 H. Cho, C. Yun and S. Yoo, *Opt. Express*, 2010, **18**, 3404–3414.
- 27 W. Shockley and H. J. Queisser, *J. Appl. Phys.*, 1961, **32**, 510–519.
- 28 S. Schubert, J. Meiss, L. Müller-Meskamp and K. Leo, *Adv. Energy Mater.*, 2013, **3**, 438–443.
- 29 D. Ebner, M. Bauch and T. Dimopoulos, *Opt. Express*, 2017, **25**, A240–A252.
- 30 Q. Jiang, L. Zhang, H. Wang, X. Yang, J. Meng, H. Liu, Z. Yin, J. Wu, X. Zhang and J. You, *Nat. Energy*, 2016, **2**, 16177.
- 31 Q. Jiang, X. Zhang and J. You, *Small*, 2018, **14**, 1801154.
- 32 S.-W. Baek, O. Ouellette, J. W. Jo, J. Choi, K.-W. Seo, J. Kim, B. Sun, S.-H. Lee, M.-J. Choi, D.-H. Nam, L. N. Quan, J. Kang, S. Hoogland, F. P. García de Arquer, J.-Y. Lee and E. H. Sargent, *ACS Energy Lett.*, 2018, **3**, 2908–2913.
- 33 Q. Xue, R. Xia, C. J. Brabec and H.-L. Yip, *Energy Environ. Sci.*, 2018, **11**, 1688–1709.
- 34 E. Della Gaspera, Y. Peng, Q. Hou, L. Spiccia, U. Bach, J. J. Jasieniak and Y.-B. Cheng, *Nano Energy*, 2015, **13**, 249–257.
- 35 G. F. Burkhard, E. T. Hoke and M. D. McGehee, *Adv. Mater.*, 2010, **22**, 3293–3297.
- 36 S. Kim and J.-L. Lee, *J. Photonics Energy*, 2012, **2**, 22.
- 37 J. Kim, O. Ouellette, O. Voznyy, M. Wei, J. Choi, M.-J. Choi, J. W. Jo, S.-W. Baek, J. Fan, M. I. Saidaminov, B. Sun, P. Li, D.-H. Nam, S. Hoogland, Z.-H. Lu, F. P. García de Arquer and E. H. Sargent, *Adv. Mater.*, 2018, **30**, 1803830.
- 38 B. Sun, O. Ouellette, F. P. García de Arquer, O. Voznyy, Y. Kim, M. Wei, A. H. Proppe, M. I. Saidaminov, J. Xu, M. Liu, P. Li, J. Z. Fan, J. W. Jo, H. Tan, F. Tan, S. Hoogland, Z. H. Lu, S. O. Kelley and E. H. Sargent, *Nat. Commun.*, 2018, **9**, 4003.
- 39 G. F. Burkhard, E. T. Hoke and M. D. McGehee, *Adv. Mater.*, 2010, **22**, 3293–3297.